

Human Trajectory Forecasting with Explainable Behavioral Uncertainty

Jiangbei Yue¹, Dinesh Manocha² and He Wang^{1*}

^{1*}University of Leeds, Woodhouse Lane, Leeds, UK.

²University of Maryland at College Park, College Park, Maryland, US.

*Corresponding author(s). E-mail(s): h.e.wang@leeds.ac.uk;

Abstract

Human trajectory forecasting helps to understand and predict human behaviors, enabling applications from social robots to self-driving cars, and therefore has been heavily investigated. Most existing methods can be divided into model-free and model-based methods. Model-free methods offer superior prediction accuracy but lack explainability, while model-based methods provide explainability but cannot predict well. Combining both methodologies, we propose a new Bayesian Neural Stochastic Differential Equation model BNSP-SFM, where a behavior SDE model is combined with Bayesian neural networks (BNNs). While the NNs provide superior predictive power, the SDE offers strong explainability with quantifiable uncertainty in behavior and observation. We show that BNSP-SFM achieves up to a 50% improvement in prediction accuracy, compared with 11 state-of-the-art methods. BNSP-SFM also generalizes better to drastically different scenes with different environments and crowd densities (~ 20 times higher than the testing data). Finally, BNSP-SFM can provide predictions with confidence to better explain potential causes of behaviors. The code will be released upon acceptance.

Keywords: Human Trajectory Forecasting, Stochastic Differential Equation, Bayesian Neural Networks, Explainable Predictions

1 Introduction

Accurate human trajectory forecasting benefits many applications, *e.g.*, social robots, self-driving vehicles, etc (Bennewitz, Burgard, & Thrun, 2002; Thrun, Burgard, & Fox, 2005), and therefore has been studied in areas from computer science, physics, and mathematics to robotics and transportation (Bendali-Braham, Weber, Forestier, Idoumghar, & Muller, 2021). Existing research largely falls into model-free and model-based methods. Model-free methods enjoy the strong data-fitting capacity of data-driven models such as statistical machine learning models (Wang, Ondřej, & O’Sullivan, 2016b; Wang & O’Sullivan,

2016) and deep neural networks (DNNs) (Goodfellow et al., 2020; Hochreiter & Schmidhuber, 1997; Kingma, Welling, et al., 2019). While they provide excellent prediction accuracy, their black-box nature makes it difficult for humans to interpret the learned underlying function. Comparatively, model-based methods are based on explicit systems parameterized as ordinary/partial/stochastic differentiable equations (O/P/SDEs) (Dietrich et al., 2021) or rule-based systems (Helbing & Molnár, 1995). These models are explainable but less accurate in prediction (Yue, Manocha, & Wang, 2022), as they do not benefit from training on data (or only on small amounts of data) and therefore are better fit in small data regime.

Overall, there seems to be a trade-off between the ability to explain (*i.e.* explainability) and the ability to predict (*i.e.* foresight).

A very recent effort has been focused on eliminating the explainability-foresight trade-off via a hybrid approach (Hossain, Johora, Müller, Hartmann, & Reinhardt, 2022; Kreiss, 2021; Yue et al., 2022). One can combine a PDE with DNNs for trajectory prediction, where the PDE can explain the behavior while the DNNs can provide data-fitting capacity. However, these approaches either do not capture uncertainty or do not explore the structure of uncertainty, only reporting the average/best performance in prediction without giving the confidence of the prediction (Alahi et al., 2016; Gupta, Johnson, Fei-Fei, Savarese, & Alahi, 2018). Generally, this is not ideal because uncertainty modeling is crucial in many tasks, especially in risk-related decision-making (Huang, McGill, Williams, Fletcher, & Rosman, 2019). Specific to human trajectories, uncertainty can also help explain behaviors better, *e.g.* why a pedestrian suddenly steers.

To fill this gap while retaining advantages of hybrid methods, we extend our previous work NSP-SFM (Yue et al., 2022) to propose a new Bayesian Neural Stochastic Differentiable Equation model for trajectory forecasting. Unlike NSP-SFM which learns a *deterministic* steering behavior plus an unexplainable randomness, we further dissect the randomness into *aleatoric uncertainty* caused by behavioral randomness and *epistemic uncertainty* by unobserved reasons (He, Xia, Zhao, & Wang, 2020). We argue that the aleatoric uncertainty should be explainable and the epistemic uncertainty can be unexplainable, because the former is observed in data and can be explained *e.g.*, due to collision avoidance, while the latter is unknown. To this end, we propose to model the steering behavior with the aleatoric uncertainty using a learnable stochastic differentiable equation and learn the epistemic uncertainty with neural nets, leading to a neural stochastic differentiable equation model. Furthermore, to quantify the level of uncertainty in the aleatoric uncertainty, we propose a Bayesian treatment on its attributed factors.

Specifically, we model the dynamics of a pedestrian trajectory as a second-order SDE, part of which modeling a learnable aleatoric uncertainty caused by stochastic social interactions among

pedestrians and stochastic interactions between a pedestrian and the environment. In addition, to account for the epistemic uncertainty, we employ a conditional variational autoencoder (CVAE) that can predict the residual between the prediction from the SDE and the observation (Yue et al., 2022). Furthermore, to quantify the randomness of the aleatoric uncertainty, we impose priors on the associated factors and learn both the motion dynamics and uncertainty via Bayesian neural networks. We call our model Bayesian Neural Social Physics (BNSP).

We show that our BNSP model can achieve the state-of-the-art performance in standard trajectory prediction tasks across several public datasets and metrics. In addition, the BNSP model can provide not only plausible explanations for predicted trajectories, but also a confidence analysis for the prediction and explanation. Moreover, we demonstrate the better generalizability to unseen scenarios of our BNSP model compared with existing methods. Formally, our contributions include:

- A new Bayesian neural stochastic differentiable equation model for trajectory forecasting and behavior analysis with fine-grained explainable uncertainties;
- A new way to combine SDE with neural networks for human trajectory prediction;
- A demonstration of the effectiveness of our model over a wide range of tasks and data: trajectory forecasting, behavior explanation with aleatoric uncertainty, generalization to unseen scenarios and high data efficiency.

2 Related Work

Human trajectory forecasting predicts future human trajectories based on historical and environmental information. Existing methods can be divided into model-based and model-free methods depending on whether it explicitly models human behaviors or not.

Model-based approaches are based on first-principles and depend on fundamental assumptions of human motions. With these assumptions, motions can be summarized into rules and deterministic systems, described as ordinary/partial differential equations or optimization problems. In such methods, velocity, acceleration and turning can be assumed to be constant (Schneider &

Gavrila, 2013) to model the steering. Pedestrians can be treated as particles that are subject to forces caused by social interactions (Helbing & Molnár, 1995). In addition to modeling people as entities, the influence of their affective states is also studied (Luo et al., 2008). Later, data-driven model-based methods are introduced to improve data fitting (Ferrer & Sanfeliu, 2014; Yan, Kakadiaris, & Shah, 2014). In such a perspective, model parameters are optimized to fit noisy data (Kim et al., 2013) and simulate the behaviors. However, model-based methods always suffer from limited flexibility of data fitting or learning capacity, making them incapable of learning from large amounts of data and predicting accurately. In comparison, our model exploits the strong data-fitting ability of deep neural networks to leverage large data fully for accurate prediction.

More recently, model-free methods based on deep learning have dominated human trajectory forecasting by demonstrating their surprisingly high prediction accuracy. Social LSTM (Alahi et al., 2016) uses Long Short-Term Memory (LSTM) networks to model social interactions and learn from temporal data. This work inspires other methods based on recurrent neural networks (Bartoli, Lisanti, Ballan, & Del Bimbo, 2018; Vemula, Muelling, & Oh, 2018; P. Zhang, Ouyang, Zhang, Xue, & Zheng, 2019) and more recent applications of transformers (Giuliani, Hasan, Cristani, & Galasso, 2021; Wong et al., 2022; Yu, Ma, Ren, Zhao, & Yi, 2020). In addition, other deep neural networks have also been explored. Deep generative models such as generative adversarial networks and variational autoencoders are exploited to handle uncertainties in the future trajectories and generate multiple acceptable predictions (Gupta et al., 2018; Ivanovic & Pavone, 2019; Kosaraju et al., 2019; Mangalam et al., 2020; Xu, Hayet, & Karamouzas, 2022). Graph and temporal convolutional neural networks provide a novel, efficient way to model interactions between people (Mohamed, Qian, Elhoseiny, & Claudel, 2020; Shi et al., 2021). Besides high prediction accuracy, it is found that these models have limited explainability and cannot generalize to drastically different scenarios well (Yue et al., 2022). Different from existing deep learning methods, our model not only provides higher accuracy in prediction but also possesses explainability

and better generalizability, benefiting from our embedded explicit model.

Very recently, hybrid approaches combining model-based and model-free methods have emerged. Physical models are embedded into deep neural networks (Hossain et al., 2022; Kreiss, 2021; Yue et al., 2022) to balance explainability and prediction accuracy. Our method falls into this category. Compared with these approaches, our model further explores the fine-grained structure of uncertainty, *i.e.*, aleatoric and epistemic uncertainty. As a result, our model can provide more accurate prediction, stronger explainability and better generalization in different scenarios.

At a high level, our method is part of a recent attempt in physics-based deep learning (Karniadakis et al., 2021) to combine deep neural networks with differential equations. Existing applications include finite element mesh generation (Z. Zhang, Jimack, & Wang, 2021; Z. Zhang, Wang, Jimack, & Wang, 2020), reduced-order modeling (Shen et al., 2021), differentiable simulation (Gong, Zhu, Andrew, & Wang, 2022), *etc.* Compared with these methods, our research focuses on human trajectory forecasting.

3 Methodology

We first introduce the background of Bayesian neural stochastic differential equations in Sec. 3.1. Then we introduce a new Stochastic Social Physics model in Sec. 3.2. Next, we introduce a new Bayesian treatment on our stochastic social physics model to derive our general Bayesian Social Physics Model (BNSP) as a general framework in Sec. 3.3. Further, we instantiate our BNSP with a stochastic social force model by augmenting a previous deterministic social force method into a stochastic one in Sec. 3.4. Finally, we derive the inference method in Sec. 3.5 and provide the implementation details in Sec. 3.6.

3.1 Background

Bayesian neural stochastic differential equation (Li, Wong, Chen, & Duvenaud, 2020; Opper, 2019; Tzen & Raginsky, 2019) is an extension and a combination of both Bayesian neural networks (Jospin, Laga, Boussaid, Buntine, & Bennamoun, 2022) and stochastic differential equations (SDEs) (Dietrich et al., 2021) that

allows for the integration of uncertainty quantification and model-based representation of dynamical systems. In this approach, neural networks are used to approximate the solution of a SDE, and Bayesian inference is used to estimate the parameters of these neural networks. This results in a probabilistic model that captures both the dynamics of the system and the uncertainty associated with the model parameters. Bayesian neural stochastic differential equation models have applications in various fields, including finance, physics, and biology. They can be used for tasks such as prediction, parameter estimation, and control of dynamic systems. The ability to model uncertainty in the dynamics of these systems makes these models particularly useful for behavioral analysis under uncertainty.

A SDE is a differential equation that includes a stochastic component and can capture the randomness inherent to dynamical systems. A typical SDE describes a system evolving over time with random fluctuations:

$$d\mathbf{X}_t = \boldsymbol{\mu}(t, \mathbf{X}_t)dt + \boldsymbol{\sigma}(t, \mathbf{X}_t)d\mathbf{W}_t, \quad (1)$$

where \mathbf{X}_t is a stochastic process of the system state, $\boldsymbol{\mu}, \boldsymbol{\sigma}$ are two real-valued functions and $\mathbf{W}(t)$ is a Wiener process. From Eq. (1), we have its integral form:

$$\begin{aligned} \mathbf{X}_{t+s} - \mathbf{X}_t &= \int_t^{t+s} \boldsymbol{\mu}(u, \mathbf{X}_u)du \\ &+ \int_t^{t+s} \boldsymbol{\sigma}(u, \mathbf{X}_u)d\mathbf{W}_u. \end{aligned} \quad (2)$$

In contrast to ODEs/PDEs, SDEs explicitly consider the randomness whose solutions are stochastic processes. Eq. (2) demonstrates that the change of the solution \mathbf{X}_t is the sum of an ordinary Lebesgue integral of $\boldsymbol{\mu}$ (the first term) and an Itô integral (the second term). In general, we refer to the function $\boldsymbol{\mu}$ and $\boldsymbol{\sigma}$ as the drift coefficient and the diffusion coefficient, respectively. The solution \mathbf{X}_t is called the diffusion processes and satisfies the Markov property. Therefore, we can model the pedestrian motion with uncertainty from the view of SDEs, which naturally captures the uncertainty of future trajectories.

3.2 Stochastic Neural Social Physics

Notation. Assuming $\mathbf{p}^t \in \mathbb{R}^2$ is the 2D location of a pedestrian at time t , we represent the whole trajectory as a function $\mathbf{p}(t)$. In data, we assume such a trajectory is observed discretely in time $\{\mathbf{p}^0, \mathbf{p}^1, \dots, \mathbf{p}^T\}$. Therefore, $\mathbf{P} = \{\mathbf{p}_i^t\}_{i=1:N}^{t=1:T} \in \mathbb{R}^{N \times T \times 2}$ represents a set of trajectories of N pedestrians of length T . Given \mathbf{p}_i^t of the i th person, we consider his/her neighborhood set Ω_i^t which includes the indices of other nearby pedestrians, \mathbf{p}_j^t with $j \in \Omega_i^t$, all of whom influence the motion of pedestrian i . The neighborhood is also a function of time $\Omega(\mathbf{t})$.

In Neural Social Physics (NSP) (Yue et al., 2022), the state of a pedestrian at t is $\mathbf{q}=[\mathbf{p}, \dot{\mathbf{p}}]^T$, and the trajectory can be formulated as:

$$\begin{cases} d\mathbf{p}(t) = \dot{\mathbf{p}}(t)dt + \alpha(\mathbf{q}^{t:t-M}) \\ d\dot{\mathbf{p}}(t) = \mathbf{F}_{goal} + \mathbf{F}_{col} + \mathbf{F}_{env}, \end{cases} \quad (3)$$

where $\mathbf{F}_{goal}, \mathbf{F}_{col}, \mathbf{F}_{env}$ are *deterministic* forces parameterized by neural networks to model social interactions. $\alpha(\mathbf{q}^{t:t-M})$ is another neural network to take into account any randomness that has not been captured in $d\dot{\mathbf{p}}(t)$. Although NSP shows superior performance, it ignores the fine-grained structure of the randomness in the data and simply captures it in $\alpha(\mathbf{q}^{t:t-M})$.

We propose to divide the randomness into aleatoric and epistemic uncertainty and learn them separately in trajectory forecasting. This is because these two uncertainties come from different sources and bear different meanings. Aleatoric uncertainty arises from the steering behavior which is random *e.g.* when avoiding other pedestrians or obstacles, while epistemic uncertainty is caused by unknown factors *e.g.* affective state, sensor error, *etc.* (He et al., 2020). Explicitly capturing the aleatoric uncertainty can help explain the behavior as well as give confidence about the prediction.

To this end, we model the aleatoric uncertainty as *random* forces rising from social interactions. We first formulate the dynamics of a person (agent) in a crowd as:

$$\begin{cases} d\mathbf{p}(t) = \dot{\mathbf{p}}(t)dt \\ d\dot{\mathbf{p}}(t) = \mathbf{f}_{\eta, \phi}(t, \mathbf{p}(t), \dot{\mathbf{p}}(t), \Omega(t), \mathbf{p}^T, \mathbf{E})dt \\ \quad + \boldsymbol{\sigma}_{\eta, \phi}(t, \mathbf{p}(t), \dot{\mathbf{p}}(t), \Omega(t), \mathbf{p}^T, \mathbf{E})d\mathbf{W}(t) \\ \mathbf{p}(0) = \mathbf{p}^0, \dot{\mathbf{p}}(0) = \dot{\mathbf{p}}^0, \mathbf{p}(T) = \mathbf{p}^T \end{cases} \quad (4)$$

given the initial position \mathbf{p}^0 , initial velocity $\dot{\mathbf{p}}^0$ and the destination \mathbf{p}^T . Here $\dot{\mathbf{p}}(t)$ and $d\dot{\mathbf{p}}(t)$ denote the first-order and the second-order dynamics of positions $\mathbf{p}(t)$. \mathbf{f} and $\boldsymbol{\sigma}$ are functions governing the dynamics. $\mathbf{W}(t)$ is a Wiener process such that for any $t_2 > t_1$, $\mathbf{W}(t_2) - \mathbf{W}(t_1)$ is normally distributed with mean 0 and variance $t_2 - t_1$. η is the set of explainable parameters and ϕ is the set of unexplainable parameters such as neural network weights. $\boldsymbol{\Omega}(t)$ represents the neighborhood set. \mathbf{E} is the environment (*e.g.*, obstacles). From Eq. 4:

$$\begin{aligned} \mathbf{p}^T - \mathbf{p}^0 &= \int_{t=0}^T \dot{\mathbf{p}}(t) dt \\ &= \int_{t=0}^T \left(\int \mathbf{f} dt + \int \boldsymbol{\sigma} d\mathbf{W}(t) \right) dt. \end{aligned} \quad (5)$$

where \mathbf{f} is a deterministic steering behavior and $\boldsymbol{\sigma} \Delta W(t)$ is the steering randomness. Eq. 4 explicitly considers the aleatoric uncertainty, but it alone cannot fully describe the motion. Therefore, we add another term, $\boldsymbol{\varepsilon}(t, \mathbf{p}^{t:t-M})$, to model the epistemic uncertainty, which is time-dependent and depends on the brief history $\mathbf{p}^{t:t-M}$ where M is the length of the history. Therefore, the full model becomes:

$$\begin{cases} d\mathbf{p}(t) = \dot{\mathbf{p}}(t) dt + \boldsymbol{\varepsilon}(t, \mathbf{p}^{t:t-M}) \\ d\dot{\mathbf{p}}(t) = \mathbf{f}_{\eta, \phi}(t, \mathbf{p}(t), \dot{\mathbf{p}}(t), \boldsymbol{\Omega}(t), \mathbf{p}^T, \mathbf{E}) dt \\ \quad + \boldsymbol{\sigma}_{\eta, \phi}(t, \mathbf{p}(t), \dot{\mathbf{p}}(t), \boldsymbol{\Omega}(t), \mathbf{p}^T, \mathbf{E}) d\mathbf{W}(t) \end{cases} \quad (6)$$

where we omit the boundary conditions. To fit this model to discrete observations in time, we discretize Eq. 6 into:

$$\begin{cases} \mathbf{p}^{t+\Delta t} - \mathbf{p}^t = \dot{\mathbf{p}}^{t+\Delta t} \Delta t + \boldsymbol{\varepsilon}^t, \mathbf{p}^{t:t-M} \\ \dot{\mathbf{p}}^{t+\Delta t} - \dot{\mathbf{p}}^t = \mathbf{f}_{\eta, \phi}(t, \mathbf{p}(t), \dot{\mathbf{p}}(t), \boldsymbol{\Omega}(t), \mathbf{p}^T, \mathbf{E}) \Delta t \\ \quad + \boldsymbol{\sigma}_{\eta, \phi}(t, \mathbf{p}(t), \dot{\mathbf{p}}(t), \boldsymbol{\Omega}(t), \mathbf{p}^T, \mathbf{E}) \Delta \mathbf{W}(t). \end{cases}$$

Finally, the full forward model is:

$$\mathbf{p}^{t+\Delta t} = \mathbf{p}^t + \dot{\mathbf{p}}^t \Delta t + \mathbf{f} \Delta t^2 + \boldsymbol{\sigma} \Delta t \Delta \mathbf{W}(t) + \boldsymbol{\varepsilon}^t, \mathbf{p}^{t:t-M} \quad (7)$$

Equation (7) is the main (stochastic) prediction model employed in this paper. It is a general model and can ideally incorporate any \mathbf{f} with a second-order differentiability. We instantiate it later.

3.3 Bayesian Neural Social Physics

A key difference between our method and previous ones is we aim to quantify the aleatoric uncertainty, through estimating the explainable parameters η in Eq. (6) during inference. To this end, we propose a Bayesian treatment on them. Note we temporally ignore unexplainable parameters ϕ as they are fixed once learned. Given a new brief history $\hat{\mathbf{p}}^h = \{\hat{\mathbf{p}}^0, \hat{\mathbf{p}}^1, \dots, \hat{\mathbf{p}}^{t_h}\}$, we predict the future trajectory $\hat{\mathbf{p}}^f = \{\hat{\mathbf{p}}^{t_h+1}, \hat{\mathbf{p}}^{t_h+2}, \dots, \hat{\mathbf{p}}^{t_h+t_f}\}$ in the testing phase. A Bayesian predictor can be represented as:

$$\begin{aligned} p(\mathbf{P}, \hat{\mathbf{p}}^h, \hat{\mathbf{p}}^f) &= \int p(\mathbf{P}, \hat{\mathbf{p}}^h, \hat{\mathbf{p}}^f, \eta) d\eta = \\ &= \int p(\hat{\mathbf{p}}^f | \hat{\mathbf{p}}^h, \mathbf{P}, \eta) p(\hat{\mathbf{p}}^h, \mathbf{P}, \eta) d\eta = \\ &= \int p(\hat{\mathbf{p}}^f | \hat{\mathbf{p}}^h, \eta) p(\eta | \mathbf{P}) p(\mathbf{P}) p(\hat{\mathbf{p}}^h) d\eta = \\ &= \int p(\hat{\mathbf{p}}^f | \hat{\mathbf{p}}^h, \eta) p(\eta | \mathbf{P}) d\eta, \end{aligned} \quad (8)$$

where η is a latent variable. $p(\hat{\mathbf{p}}^f | \hat{\mathbf{p}}^h, \mathbf{P}, \eta) = p(\hat{\mathbf{p}}^f | \hat{\mathbf{p}}^h, \eta)$ because \mathbf{P} is given and not part of the prediction process. $p(\hat{\mathbf{p}}^h, \mathbf{P}, \eta) = p(\eta | \hat{\mathbf{p}}^h, \mathbf{P}) p(\hat{\mathbf{p}}^h, \mathbf{P}) = p(\eta | \mathbf{P}) p(\hat{\mathbf{p}}^h) p(\mathbf{P}) = p(\eta | \mathbf{P})$ as $\hat{\mathbf{p}}^h$ is not used for estimating η , and $\hat{\mathbf{p}}^h$ and \mathbf{P} are observed. After learning $p(\eta | \mathbf{P})$, the model predicts via $p(\hat{\mathbf{p}}^f | \hat{\mathbf{p}}^h, \eta)$ across all η . With Bayesian inference to learn $p(\eta | \mathbf{P})$, we obtain our full framework BNSP by using Eq. (7) for $p(\hat{\mathbf{p}}^f | \hat{\mathbf{p}}^h, \eta)$. BNSP benefits from the quantification of uncertainty during prediction.

Remarks. Most existing deep learning methods can be represented as Eq. (8), where $p(\hat{\mathbf{p}}^f | \hat{\mathbf{p}}^h, \eta)$ is realized as neural networks (NNs) parameterized by learned parameters (Alahi et al., 2016; Gupta et al., 2018; Mangalam, An, Girase, & Malik, 2021). Deviating from these unexplainable models, recently some research (Hossain et al., 2022; Kreiss, 2021; Yue et al., 2022) shows that $p(\hat{\mathbf{p}}^f | \hat{\mathbf{p}}^h, \eta)$ can be realized as ODEs/PDEs with model parameters and motion randomness captured by NNs. However, while the ODEs/PDEs provide explainability to some extent, they are intrinsically deterministic so that the randomness is either not captured or still captured by additional neural network components hence unexplainable. Their learned randomness does not

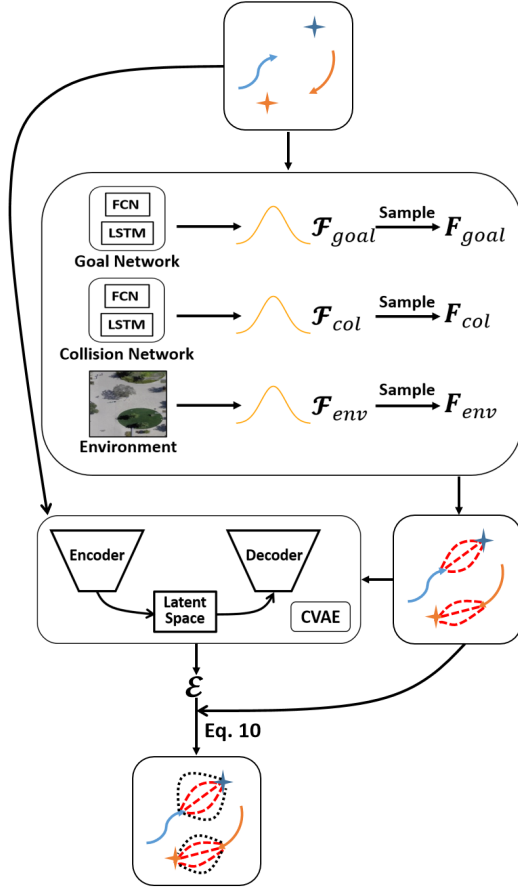


Fig. 1 Overview of BNSP-SFM. \mathcal{F}_{goal} and \mathcal{F}_{col} are estimated at each step through the attraction network and the evasion network. \mathcal{F}_{env} is a normal distribution related to the environment with the learnable mean and variance. For every step, we sample $\mathbf{F}_{goal}^t \sim \mathcal{F}_{goal}^t$, $\mathbf{F}_{col}^t \sim \mathcal{F}_{col}^t$ and $\mathbf{F}_{env}^t \sim \mathcal{F}_{env}^t$ and sample an observational noise ε from the CVAE, then predict the future position via Eq. (10).

truly capture the posterior $p(\eta \mid \mathbf{P})$. Explicitly capturing and explaining such uncertainty is crucial for analysis and prediction, which can be naturally captured by Bayesian inference, as proposed by us.

3.4 Instantiation of BNSP with Stochastic Social Forces

Similar to (Yue et al., 2022), we instantiate f using social forces (Helbing & Molnár, 1995) but augment it with stochastic forces instead of deterministic ones. One key difference in the modeling choice between our model (Eq. (6)) and NSP-SFM (Yue et al., 2022) (Eq. (3)) is that NSP-SFM assumes all the randomness happens

at the first-order, while BNSP assumes the epistemic uncertainty is captured at the first order but the aleatoric uncertainty is captured at the second order, which is more sensible as this is where the stochastic forces caused by social interactions are modeled. We name our model BNSP-SFM.

Similar to Eq. (3), we consider three main factors for the behavior in Eq. (7): stochastic goal attraction \mathcal{F}_{goal} , stochastic collision avoidance \mathcal{F}_{col} and stochastic environment repulsion \mathcal{F}_{env} . To this end, we specify the second-order part of Eq. (7) as:

$$\mathbf{f} + \sigma \frac{\Delta W(t)}{\Delta t} = \mathcal{F}_{goal} + \mathcal{F}_{col} + \mathcal{F}_{env}, \quad (9)$$

Substituting Eq. (9) into Eq. (7) gives:

$$\begin{aligned} \mathbf{p}^{t+\Delta t} &= \mathbf{p}^t + \dot{\mathbf{p}}^t \Delta t + \\ &(\mathbf{F}_{goal}^t + \mathbf{F}_{col}^t + \mathbf{F}_{env}^t) \Delta t^2 + \varepsilon^t \cdot \mathbf{p}^{t-t-M} \quad (10) \\ \mathbf{F}_{goal}^t &\sim \mathcal{F}_{goal}^t, \mathbf{F}_{col}^t \sim \mathcal{F}_{col}^t, \mathbf{F}_{env}^t \sim \mathcal{F}_{env}^t, \end{aligned}$$

where \mathcal{F}_{goal} and \mathcal{F}_{col} are time-varying Gaussians. \mathcal{F}_{env} is a static Gaussian. The overview of our model is shown in Figure 1. After training, given an input trajectory and an endpoint, we predict distributions \mathcal{F}_{goal}^t , \mathcal{F}_{col}^t and \mathcal{F}_{env}^t by neural networks; then we can sample $\mathbf{F}_{goal}^t \sim \mathcal{F}_{goal}^t$, $\mathbf{F}_{col}^t \sim \mathcal{F}_{col}^t$, $\mathbf{F}_{env}^t \sim \mathcal{F}_{env}^t$ and $\varepsilon^t \cdot \mathbf{p}^{t-t-M}$ at time t . Iteratively, we can predict positions via solving Eq. (10). Note that, in Eq. (6), we assume that destinations \mathbf{p}^T are given, although they are not available directly during prediction. Therefore, we employ the pre-trained Goal Sampling Network (GSN) (Yue et al., 2022) to sample \mathbf{p}^T in advance for prediction during testing.

3.4.1 Individual Neural Networks

Stochastic Goal Attraction Humans are constantly attracted to their destinations. However, the magnitude and direction of such an attraction can vary over time and in different circumstances (*e.g.*, detour for collision avoidance). We model such goal attraction as a stochastic force:

$$\begin{aligned} \mathbf{F}_{goal}^t &= \left(\frac{\mathbf{p}^T - \mathbf{p}^t}{(T-t)\Delta t} - \dot{\mathbf{p}}^t \right) k_{goal}^t \quad (11) \\ k_{goal}^t &\sim \mathcal{N}_{\phi_1}(\mu_{goal}^t, \sigma_{goal}^t{}^2), \end{aligned}$$

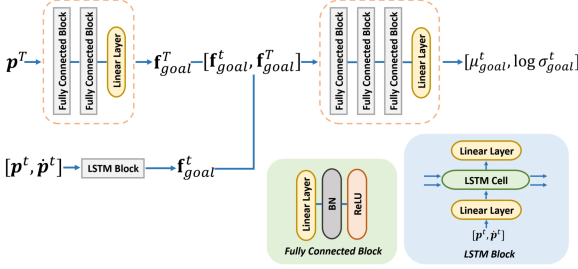


Fig. 2 The structure of the goal network.

where $(\frac{\mathbf{p}^T - \mathbf{p}^t}{(T-t)\Delta t} - \dot{\mathbf{p}}^t)$ is the expected velocity correction on the current velocity $\dot{\mathbf{p}}^t$ towards \mathbf{p}^T . μ_{att}^t and σ_{att}^t are the mean and standard deviation functions at t , realized by the Goal Network (GN) with parameters ϕ_1 :

$$[\mu_{goal}^t, \sigma_{goal}^t]_{\phi_1} = GN_{\phi_1}(\mathbf{p}^t, \dot{\mathbf{p}}^t, \mathbf{p}^T) \quad (12)$$

whose architecture is shown in Fig. 2. $[\mathbf{p}^t, \dot{\mathbf{p}}^t]$ is encoded and fed into a Long Short-Term Memory (LSTM) network (Hochreiter & Schmidhuber, 1997). The output of the LSTM is transformed by a linear layer to get the feature \mathbf{f}_{goal}^t . The first orange block (orange dashed lines), which consists of two fully connected blocks and one linear layer, is used to encode the destination \mathbf{p}^T into \mathbf{f}_{goal}^T . Then the concatenated feature $[\mathbf{f}_{goal}^t, \mathbf{f}_{goal}^T]$ is fed into the second orange block to output the distribution parameters $[\mu_{k_{goal}}^t, \log \sigma_{k_{goal}}^t]$. Instead of learning $\sigma_{k_{goal}}$ directly, we learn its logarithm to ensure that every output dimensions have the same range. The dimensions of each linear layer in the first and second orange block are $[64, 256, 16]$ and $[512, 256, 512, 2]$, respectively. In the LSTM block, the linear layers before and after the LSTM have dimensions 64 and 16, respectively. We use an LSTM with 256 dimensions.

Stochastic Collision Avoidance Given the i th pedestrian at t , \mathbf{p}_i^t , its neighborhood Ω_i^t and any pedestrian \mathbf{p}_j^t , $j \in \Omega_i^t$, we define the collision avoidance factor \mathcal{F}_{col}^t as follows:

$$\begin{aligned} \mathcal{F}_{col}^t &= \sum_{j=0}^m \mathcal{F}_{col_{ij}}^t, \text{ where } j \in \Omega_i^t, \mathbf{F}_{col_{ij}}^t \sim \mathcal{F}_{col_{ij}}^t \\ \mathbf{F}_{col_{ij}}^t &= -\nabla_{\mathbf{r}_{ij}^t} r_{col} e^{-\|\mathbf{r}_{ij}^t\|/r_{col}} k_{col_{ij}}^t, \\ \mathbf{r}_{ij} &= \mathbf{p}_i^t - \mathbf{p}_j^t, k_{col_{ij}}^t \sim \mathcal{N}_{\phi_2}(\mu_{col_{ij}}^t, \sigma_{col_{ij}}^t{}^2), \end{aligned} \quad (13)$$

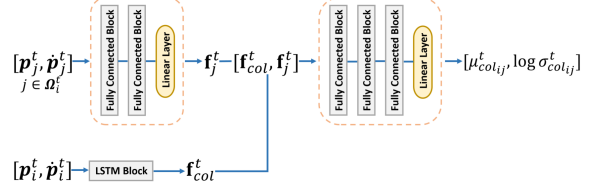


Fig. 3 The structure of the collision network.

where $\mu_{eva_{ij}}^t$ and $\sigma_{eva_{ij}}^t$ are the mean and standard deviation functions. Similar to (Helbing & Molnár, 1995), $r_{col} e^{-\|\mathbf{r}_{ij}\|/r_{col}}$ is a repulsive potential energy function with a radius r_{col} (hyperparameter), and the negative gradient w.r.t. r_{ij} gives a repulsive force. However, such repulsion between pedestrians has randomness (He et al., 2020; Wang, Ondřej, & O’Sullivan, 2016a). Therefore, our model considers a time-varying Gaussian with learnable mean and variance, so that the collision avoidance factor \mathcal{F}_{col}^t is a time-varying Gaussian mixture. We realize $\mu_{col_{ij}}$ and $\sigma_{col_{ij}}$ by the Collision Network (CN) parameterized by ϕ_2 :

$$[\mu_{col_{ij}}^t, \sigma_{col_{ij}}^t]_{\phi_2} = CN_{\phi_2}(\mathbf{p}_i^t, \dot{\mathbf{p}}_i^t, \mathbf{p}_j^t, \dot{\mathbf{p}}_j^t) \quad (14)$$

whose architecture is shown in Fig. 3. For any neighbor \mathbf{p}_j^t in Ω_i^t , the collision network encodes $[\mathbf{p}_i^t, \dot{\mathbf{p}}_i^t]$ and $[\mathbf{p}_j^t, \dot{\mathbf{p}}_j^t]$ to features \mathbf{f}_{col}^t and \mathbf{f}_j^t , respectively. The concatenated feature $[\mathbf{f}_{col}^t, \mathbf{f}_j^t]$ is fed into a decoder to output the distribution parameters. The collision network has the same architecture and dimensions as the goal network except that the input dimension of the first orange block is 4.

Stochastic Environment Repulsion To model how people avoid obstacles in the environment, given the position \mathbf{p}^t and an obstacle position \mathbf{p}_{obj} , we define the repulsion as:

$$\begin{aligned} \mathcal{F}_{env}^t &= \sum_{obj \in \mathbf{E}} \mathcal{F}_{obj}^t, \mathbf{F}_{obj}^t \sim \mathcal{F}_{obj}^t \\ \mathbf{F}_{obj}^t &= \left(\frac{\mathbf{p}^t - \mathbf{p}_{obj}}{\|\mathbf{p}^t - \mathbf{p}_{obj}\|_2} \right) k_{env}, k_{env} \sim \mathcal{N}(\mu_{obj}, \sigma_{obj}^2) \end{aligned} \quad (15)$$

where μ_{obj} and σ_{obj} are the mean and standard deviation. Different from Eq. (11) and Eq. (13), k_{env} is assumed to be time-independent and agent-independent. This is because we observe similar influences of obstacles on different pedestrians.

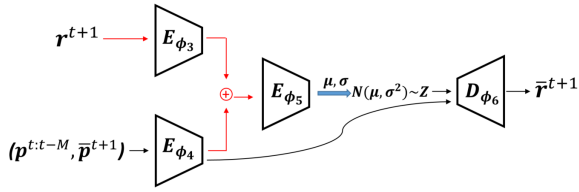


Fig. 4 The Structure of CVAE. The residual $\mathbf{r}^{t+1} = \mathbf{p}^{t+1} - \bar{\mathbf{p}}^{t+1}$. E_{ϕ_3} , E_{ϕ_4} , E_{ϕ_5} and D_{ϕ_6} are all multi-layer perceptrons. The red connections are only used in the training phase.

Therefore, unlike \mathcal{F}_{att} and \mathcal{F}_{col} , we learn μ_{obj} and σ_{obj} directly and do not use neural networks.

Epistemic Uncertainty

Finally, we specify the epistemic uncertainty term $\varepsilon^{t, \mathbf{P}^{t:t-M}}$. Here, we employ the same strategy as (Yue et al., 2022) and assume the observation noise has a well-behaved distribution in the latent space, rather than the data space. This is because the epistemic term captures all the residual randomness that is not captured by Eq. (4) and its distribution is arbitrary. Therefore, we use a variational autoencoder to learn its distribution. The architecture of the Conditional Variational Autoencoder (CVAE) is shown in Fig. 4. We use the CVAE to reconstruct the residual $\mathbf{r}^{t+1} = \mathbf{p}^{t+1} - \bar{\mathbf{p}}^{t+1}$ between the ground truth \mathbf{p}^{t+1} and the prediction $\bar{\mathbf{p}}^{t+1}$ only considering the aleatoric uncertainty. The residual \mathbf{r}^{t+1} is encoded by E_{ϕ_3} , while the history condition $(\mathbf{p}^{t:t-M}, \bar{\mathbf{p}}^{t+1})$ is encoded by another encoder E_{ϕ_4} . Their outputs are concatenated and then fed into the encoder E_{ϕ_5} to output means and variances of the Gaussian distribution of the latent variable \mathbf{Z} . Then we sample \mathbf{Z} and concatenate it with the feature of the history condition to generate the input of the decoder D_{ϕ_6} . Finally, the decoder D_{ϕ_6} computes the predicted residual.

The red connections in Fig. 4 are only used in the training phase. The ground truth \mathbf{r}^{t+1} is unavailable during the testing phase. We sample the latent variable \mathbf{Z} from a Gaussian distribution $\mathcal{N}(0, \sigma_{latent} \mathbf{I})$ with a hyper-parameter σ_{latent} . We extract the history feature from the history condition through the trained encoder E_{ϕ_4} . Then we concatenate sampled \mathbf{Z} and the history feature to decode via the trained decoder D_{ϕ_6} to obtain the estimated residual. The neural networks E_{ϕ_3} , E_{ϕ_4} , E_{ϕ_5} , and D_{ϕ_6} are all multi-layer perceptrons (MLPs). The dimensions of neural networks

Table 1 Details of the CVAE. The dimensions of every MLP and the values of hyper-parameters in the CVAE are demonstrated.

	Dimensions or Values
E_{ϕ_3}	[2, 8, 16, 16]
E_{ϕ_4}	[18, 512, 256, 16]
E_{ϕ_5}	[32, 8, 50, 32]
D_{ϕ_6}	[32, 1024, 512, 1024, 2]
M	7
σ_{latent}	1.3

and the values of hyper-parameters are shown in Tab. 1.

3.5 Loss Function and Bayesian Inference

Now we are ready to derive the loss function for our BNSP-SFM model to learn the posterior $p(\eta | \mathbf{P}) \propto p(\mathbf{P} | \eta)p(\eta)$, where $p_\phi(\mathbf{P} | \eta)$ is a doubly stochastic differential equation (Eq. (7)). Here, \mathbf{P} denotes the training set and $\eta = \{k_{goal}, k_{col_{i,j}}, k_{env}\}$ is directly explainable. In addition, the distributions are parameterized by $\phi = \phi_{\mathbf{F}} \cup \phi_{\varepsilon} = \{\phi_1, \phi_2, \mu_{obj}, \sigma_{obj}\} \cup \{\phi_3, \phi_4, \phi_5, \phi_6\}$, which includes unexplainable network weights and distribution parameters that cannot be explained directly. Our learning scheme consists of two parts depending on two losses \mathcal{L}_{Bayes} and \mathcal{L}_{cvae} . We use Bayesian inference (Blundell, Cornebise, Kavukcuoglu, & Wierstra, 2015) to derive \mathcal{L}_{Bayes} because the integral on $p(\eta)$ is intractable to learn $p(\eta | \mathbf{P})$ directly. Specifically, we minimize the KL divergence between a variational posterior $q_{\phi_{\mathbf{F}}}(\eta)$ and the true posterior $p(\eta | \mathbf{P})$:

$$\begin{aligned}
 \phi_{\mathbf{F}} &= \underset{\phi_{\mathbf{F}}}{\operatorname{argmin}} D_{\text{KL}}(q_{\phi_{\mathbf{F}}}(\eta) \| p(\eta | \mathbf{P})) \\
 &= \underset{\phi_{\mathbf{F}}}{\operatorname{argmin}} \mathbb{E}_{q_{\phi_{\mathbf{F}}}(\eta)} \left[\log q_{\phi_{\mathbf{F}}}(\eta) - \log \left(\frac{p(\mathbf{P} | \eta)p(\eta)}{p(\mathbf{P})} \right) \right] \\
 &= \underset{\phi_{\mathbf{F}}}{\operatorname{argmin}} \{ \mathbb{E}_{q_{\phi_{\mathbf{F}}}(\eta)} [\log q_{\phi_{\mathbf{F}}}(\eta) - \log p(\mathbf{P} | \eta)p(\eta)] \\
 &\quad + \underbrace{\log p(\mathbf{P})}_{\text{const}} \} \\
 &= \underset{\phi_{\mathbf{F}}}{\operatorname{argmin}} \underbrace{\mathbb{E}_{q_{\phi_{\mathbf{F}}}(\eta)} [\log q_{\phi_{\mathbf{F}}}(\eta) - \log p(\mathbf{P} | \eta)p(\eta)]}_{\mathcal{L}_{Bayes}(\phi_{\mathbf{F}} | \mathbf{P}, \eta)},
 \end{aligned} \tag{16}$$

where we assume that both of $q_{\phi_{\mathbf{F}}}(\eta)$ and $p(\eta)$ are diagonal Gaussian distributions. Then we can get:

$$\begin{aligned}\log q_{\phi_{\mathbf{F}}}(\eta) &= \sum_{k \in \eta} -\frac{(k - \mu_{\phi_{\mathbf{F}}})^2}{2\sigma_{\phi_{\mathbf{F}}}^2} - \log \sigma_{\phi_{\mathbf{F}}} - \log \sqrt{2\pi} \\ \log p(\eta) &= \sum_{k \in \eta} -\frac{(k - \mu_{prior})^2}{2\sigma_{prior}^2} - \log \sigma_{prior} - \log \sqrt{2\pi},\end{aligned}\quad (17)$$

where $\mu_{\phi_{\mathbf{F}}}$ and $\sigma_{\phi_{\mathbf{F}}}^2$ are the means and variances predicted by our method with parameters $\phi_{\mathbf{F}}$ for each $k \in \eta$. We empirically choose the prior for training. We also model the likelihood $p(\mathbf{P} | \eta)$ as a diagonal Gaussian:

$$\log p(\mathbf{P} | \eta) = \sum_{\mathbf{p}^f \in \mathbf{P}} -\frac{1}{2} \|\bar{\mathbf{p}}^f - \mathbf{p}^f\|_2^2 - \frac{t_f}{2} \log 2\pi, \quad (18)$$

where $\bar{\mathbf{p}}^f = \{\bar{\mathbf{p}}^{t_h+1}, \bar{\mathbf{p}}^{t_h+2}, \dots, \bar{\mathbf{p}}^{t_h+t_f}\}$ is calculated via Eq. (4) given η and $\mathbf{p}^h = \{\mathbf{p}^0, \mathbf{p}^1, \dots, \mathbf{p}^{t_h}\}$, and \mathbf{p}^f is the ground truth. We optimize $\phi_{\mathbf{F}}$ using \mathcal{L}_{Bayes} . This learns the parameters that are not in the CVAE.

Then we train the CVAE by using:

$$\begin{aligned}\mathcal{L}_{cvae} &= \frac{1}{N t_f} \sum_{i=1}^N \sum_{t=t_h+1}^{t_h+t_f} \{\|\mathbf{r}_i^t - \bar{\mathbf{r}}_i^t\|_2^2 \\ &\quad + \lambda D_{\text{KL}}(q_{\phi_5}(\mathbf{z}_i^t | E_{\phi_3}, E_{\phi_4}) \| \mathcal{N}(0, \mathbf{I}))\},\end{aligned}\quad (19)$$

where N is the total number of data samples, λ is a tradeoff hyper-parameter, $\mathbf{r}_i^t = \mathbf{p}_i^t - \bar{\mathbf{p}}_i^t$ is the residual and $\bar{\mathbf{r}}_i^t$ is the predicted residual out of p_{ϕ_6} . Our overall loss function is $\mathcal{L} = \mathcal{L}_{Bayes} + \mathcal{L}_{cvae}$.

3.6 Implementation Details

We first pre-train the model without the epistemic uncertainty by using \mathcal{L}_{Bayes} to ensure that the aleatoric uncertainty captures most of the behavior, then train the CVAE via \mathcal{L}_{cvae} while fixing other parameters. Details are shown in Algorithm 1.

We use ADAM for training. The learning rates for the attraction network, the evasion network, and the environment distribution are between 3×10^{-6} and 3×10^{-5} . The learning rates for CVAE are between 1×10^{-7} and 1×10^{-6} .

Algorithm 1 Training strategy

Parameters:

Goal Network (ϕ_1)
Collision Network (ϕ_2)
Environment Distribution ($\{\mu_{obj}, \sigma_{obj}\}$)
CVAE($\{\phi_3, \phi_4, \phi_5, \phi_6\}$)

Phase 1: Only Aleatoric Uncertainty

while not converged do

1 Train ϕ_1 via \mathcal{L}_{Bayes} while fixing $\{\phi_2, \mu_{obj}, \sigma_{obj}\}$

2 Train $\{\phi_2, \mu_{obj}, \sigma_{obj}\}$ via \mathcal{L}_{Bayes} while fixing ϕ_1

end while

Phase 2: Add Epistemic Uncertainty

while not converged do

Train $\{\phi_3, \phi_4, \phi_5, \phi_6\}$ via \mathcal{L}_{cvae}
while fixing $\{\phi_1, \phi_2, \mu_{obj}, \sigma_{obj}\}$

end while

4 Experiments

4.1 Datasets

We use two public datasets for evaluation: SDD (Robicquet, Sadeghian, Alahi, & Savarese, 2016) and ETH/UCY (Lerner, Chrysanthou, & Lischinski, 2007; Pellegrini, Ess, & Gool, 2010), which are widely used in human trajectory forecasting. **Stanford Drone Dataset (SDD)**: The dataset contains videos across 20 different scenes in bird’s eye view, with more than 100,000 pedestrian-pedestrian interactions and pedestrian-environment interactions. Following (Mangalam et al., 2021), we extract trajectories with a time step 0.4 seconds and obtain 20-frame samples for an 8/12 setting, i.e., given the first 8 frames (3.2 seconds, $t_h = 7$), we aim to predict the future 12 frame trajectories (4.8 seconds, $t_f = 12$). **ETH/UCY Datasets**: There are five sub-datasets (ETH, Hotel, Univ, Zara1, and Zara2), including more than 1500 pedestrians with various behaviors such as collision avoidance. Following the standard leave-one-out evaluation protocol (Gupta et al., 2018; Mangalam et al., 2021, 2020), we train our model on four sub-datasets and test it on the remaining one in turn. The world coordinates used by the dataset don’t match some parts of our model such as the goal sampling network and \mathcal{F}_{env} . Our model generally works in the pixel space. Therefore, we convert the world coordinates into pixel coordinates using

Table 2 Results on SDD based on standard-sampling. XX/XX is ADE/FDE. BNSP-SFM achieves the state-of-the-art performance in both ADE and FDE compared with all baseline methods. Reported errors are in pixels, and lower is better.

S-GAN	Sophie	P2TIRL	SimAug	PECNet	Y-net	SocialVAE	V ² -Net	NSP-SFM	Ours
27.23/41.44	16.27/29.38	12.58/22.07	10.27/19.71	9.96/15.88	7.85/11.85	8.10/11.72	7.12/11.39	6.52/10.61	6.46/10.49

Table 3 Results on ETH/UCY based on standard-sampling. XX/XX is ADE/FDE. Our model achieves the state-of-the-art results in ADE and FDE. The unit is meters, and lower is better.

	S-GAN	Sophie	NEXT	PECNet	Y-net	SocialVAE	V ² -Net	NSP-SFM	BNSP-SFM (Ours)
ETH	0.81/1.52	0.70/1.43	0.73/1.65	0.54/0.87	0.28/0.33	0.41/0.58	0.23/0.37	0.25/ 0.24	0.25/0.25
HOTEL	0.72/1.61	0.76/1.67	0.30/0.59	0.18/0.24	0.10/0.14	0.13/0.19	0.11/0.16	0.09/0.13	0.09/0.11
UNIV	0.60/1.26	0.54/1.24	0.60/1.27	0.35/0.60	0.24/0.41	0.21/0.36	0.21/0.35	0.21/0.38	0.20/0.38
ZARA1	0.34/0.69	0.30/0.63	0.38/0.81	0.22/0.39	0.17/0.27	0.17/0.29	0.19/0.30	0.16/0.27	0.16/0.27
ZARA2	0.42/0.84	0.38/0.78	0.31/0.68	0.17/0.30	0.13/0.22	0.13/0.22	0.14/0.24	0.12/0.20	0.12/0.19
AVG	0.58/1.18	0.54/1.15	0.46/1.00	0.29/0.48	0.18/0.27	0.21/0.33	0.18/0.28	0.17/0.24	0.16/0.24

the homography matrices from Y-net (Mangalam et al., 2021). We project the predictions back into the world space to calculate errors for fair comparisons with existing methods. We extract the trajectories in the same way as SDD and adopt the same 8/12 prediction strategy. For pedestrians that have less than 20 frames, we treat them as observed dynamic obstacles as part of the environment.

4.2 Trajectory Forecasting

We adopt well-established Average Displacement Error (ADE) and Final Displacement Error (FDE) (Alahi et al., 2016; Gupta et al., 2018; Yue et al., 2022) to measure the prediction accuracy. ADE is the ℓ_2 error between a predicted trajectory and its ground truth averaged over all positions, while FDE is the ℓ_2 error between the predicted destination and its ground truth. Following prior research, we report the best ADE and FDE among multiple sampled trajectories. There are two existing strategies in existing work: standard-sampling and ultra-sampling. Standard-sampling employs 20 sampled trajectories and ultra-sampling employs 20 sampled positions at each step. The former is more widely employed and the latter is employed when the model is intrinsically stochastic especially when multiple stochastic components exist (Yue et al., 2022). We compare our BNSP-SFM in both standard-sampling and ultra-sampling with a wide range of baselines: Social GAN (S-GAN) (Gupta

et al., 2018), Sophie (Sadeghian et al., 2019), NEXT (Liang, Jiang, Niebles, Hauptmann, & Fei-Fei, 2019), P2TIRL (Deo & Trivedi, 2020), SimAug (Liang, Jiang, & Hauptmann, 2020), PECNet (Mangalam et al., 2020), Y-Net (Mangalam et al., 2021), S-CSR (Zhou, Ren, Yang, Fan, & Huang, 2021), SocialVAE (Xu et al., 2022), V²-Net (Wong et al., 2022), and NSP-SFM (Yue et al., 2022).

We first show the standard-sampling results in Tab. 2 and Tab. 3. Our BNSP-SFM achieves state-of-the-art performance on both SDD and ETH/UCY. Overall, both NSP-SFM and BNSP-SFM outperform other methods. BNSP-SFM provides slightly better results than NSP-SFM. On SDD, BNSP-SFM obtains 6.46/10.49 in ADE/FDE, improving the past state-of-the-art model NSP-SFM (6.52/10.61) by 0.92%/1.13%. Compared with other previous methods, our BNSP-SFM has at least 9.27%/7.90% improvement in ADE/FDE. On ETH/UCY, the improvement is 5.88% in ADE on average and gains a better average FDE with the maximum 15.38% improvement in Hotel. Since BNSP-SFM is based on NSP-SFM, it is understandable that they can achieve similar numerical accuracy. However, the Bayesian components do not hurt prediction accuracy while providing additional explainability and confidence estimation, which are extra benefits.

Further, we show ultra-sampling results in Tab. 4. BNSP-SFM outperforms NSP-SFM by approximately 14.61%/60.17% in ADE/FDE on

Table 4 Results on ETH/UCY and SDD based on ultra-sampling. XX/XX is ADE/FDE. Our model BNSP-SFM outperforms other baselines on all datasets in ADE and FDE.

	S-CSR	NSP-SFM	BNSP-SFM (Ours)
ETH	0.19/0.35	0.07/0.09	0.05/0.04
HOTEL	0.06/0.07	0.03/0.07	0.03/0.02
UNIV	0.13/0.21	0.03/0.04	0.03/0.03
ZARA1	0.06/0.07	0.02/0.04	0.02/0.02
ZARA2	0.06/0.08	0.02/0.04	0.02/0.02
AVG	0.10/0.16	0.03/0.06	0.03/0.03
SDD	2.77/3.45	1.78/3.44	1.52/1.37

SDD. We also observe that BNSP-SFM gains the same performance in ADE and 50% improvement in FDE on ETH/UCY compared with NSP-SFM. BNSP-SFM has higher performance than S-CSR on both datasets. Stochastic models with ultra-sampling such as S-CSR and NSP-SFM have shown to be more accurate in prediction (Yue et al., 2022), but BNSP-SFM still outperform them in general. Further, for a fair comparison with S-CSR, both BNSP-SFM and NSP-SFM sample 20 destinations and only sample 15 positions at each step, so the total number of sampled trajectories is slightly smaller than S-CSR. S-CSR doesn’t need the given goals and samples 20 positions at each step following the ultra-sampling strategy. However, both BNSP-SFM and NSP-SFM outperform S-CSR. The main difference is that S-CSR is a black-box neural network based on Variational Autoencoder, while the core of BNSP-SFM and NSP-SFM are based on explicit models, which clearly demonstrates its advantages. Further, BNSP-SFM improves the accuracy or is at least in par with NSP-SFM in all scenarios, indicating that the Bayesian components manage to capture the uncertainty better and our new model retains the great prediction ability.

4.3 Generalization

4.3.1 Generalization on Cross-scene Testing

One way to test the generalizability is cross-scene testing, *i.e.*, training on one scene and testing on another, drastically different scene. Although the results on ETH/UCY and SDD are already based on cross-scene testing, we increase the challenge by using ETH/UCY and SDD as training

Table 5 Results across scenarios. All models are trained on ETH/UCY and tested on SDD. Our model achieves the best performance. Reported errors are in pixels, and lower is better.

Models	Y-net	NSP-SFM	BNSP-SFM (Ours)
ADE/FDE	30.59/51.43	6.65/10.60	6.55/10.59

and testing data respectively, where the scenes are more different in terms of the environment, space size and pedestrian dynamics. For comparison, we choose Y-net and NSP-SFM as baselines and show the results in Tab. 5. The performance of Y-net drops severely from 7.85/11.85 (when it’s trained also on SDD) to 30.59/51.43. NSP-SFM and BNSP-SFM perform slightly worse than when they are also trained on SDD, but considerably better than Y-net. NSP-SFM changes from 6.52/10.61 to 6.65/10.60 while BNSP-SFM changes from 6.46/10.49 to 6.55/10.59. This shows NSP-SFM and BNSP-SFM learn intrinsic behaviors of pedestrians that are universal across scenes.

4.3.2 Generalization to High-density Scenarios

Generalization is the ability to adapt to unseen data. Normally, we assume that the distribution of the training data is similar to that of the testing data. A model with a good generalizability should perform well not only on the testing data but also on drastically different data. For trajectory prediction methods, an efficient way to evaluate their generalizability is to use the trained model to simulate pedestrians with much higher densities, as it will lead to significantly different pedestrian dynamics (Narang, Best, Curtis, & Manocha, 2015).

Following (Yue et al., 2022), we adopt the collision rate as the metric to evaluate the generalizability. We regard each agent as a disc with a radius of r pixels. We count one collision if the minimum distance between two trajectories falls below $2r$ at any time. Given N agents in the scene, we calculate the collision rate as $R_{col} = \frac{M}{N(N-1)/2}$, where M is the number of collisions. Generally, the ground-truth r is hard to acquire because of the tracking error, the distorted images, etc. We observe unrealistically high collision rates in all cases when r is too large. In contrast, the collision rate will always be too low when r is too small,

Table 6 Collision rates on the testing data of SDD and ETH/UCY. BNSP-SFM achieves the same or better performance on all datasets.

	Y-net	S-CSR	NSP-SFM	BNSP-SFM (Ours)
ETH	0	0	0	0
HOTEL	0	0	0	0
UNIV	1.51%	1.82%	1.48%	1.48%
ZARA1	0.82%	0.41%	0	0
ZARA2	1.31%	1.31%	0.66%	0.66%
AVG	0.73%	0.71%	0.43%	0.43%
SDD	0.47%	0.42%	0.42%	0.40%

e.g., $r = 0$ will give 0% collision rate all the time. Therefore, we need to search for a reasonable r that keeps the collision rate of the ground-truth data approximately zero.

According to (Yue et al., 2022), we set the r as 7.5 pixels 0.2 m on SDD and ETH/UCY, respectively. A lower collision rate means higher plausibility and better generalization. We conduct two kinds of experiments: one is the collision rates on the testing data of SDD and ETH/UCY; the other is the collision rates on unseen scenarios with higher crowd densities. The first one compares the plausibility of predicted trajectories in scenarios similar to the training data. The second one pushes the models for generalization. We use NSP-SFM, Y-net, and S-CSR as baselines.

Collision rates on testing data (Tab. 6) show all methods achieve reasonable results, with the maximum 1.82% from S-CSR on UNIV. All methods achieve 0% in ETH and HOTEL. This is not surprising for two reasons. First, all methods predict well. So, if the ground-truth data does not contain collisions, neither do the predictions. The second reason is the sparsity of people in the scene. For instance, the highest number of people who are simultaneously in the scene is 11 in Coupa0 (in SDD). Even if the prediction goes wrong, there might not be people around, so no collisions will occur. When people are indeed close to each other, NSP-SFM and BNSP-SFM outperform Y-net and S-CSR. This is because our learned explicit model has an explicit repulsive force between agents, and can therefore avoid collisions.

To test models in drastically different scenarios from the two datasets, we select the scene Coupa0 from SDD and use the highest number of people (HNP) in the scene as an indicator of the crowd density. Coupa0 has a large space so, in theory, it can contain many people. However, the HNP

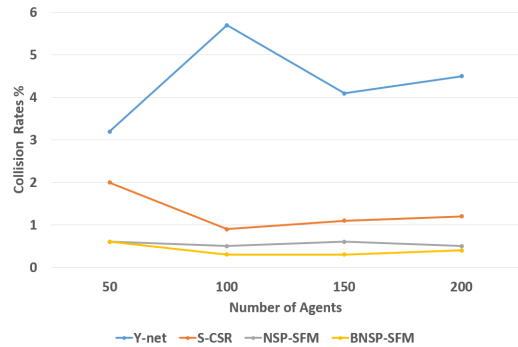


Fig. 5 The relationship between the collision rate and the number of agents. Our BNSP-SFM achieves the lowest collision rates across all settings.

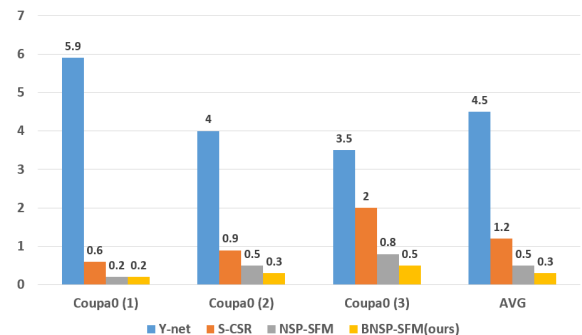


Fig. 6 Collision rates on Coupa0 with 200 HNP. Three collision rates on three intervals and their average are reported for all methods. Our BNSP-SFM outperforms all baseline methods and shows the stronger generalizability. The unit for the vertical axis is percentage.

in the original Coupa0 is merely 11. Therefore, we increase the HNP to 50, 100, 150, and 200 people. Then we use all methods trained on the original SDD data as simulators to run a long simulation and compute the collision rates for three time intervals of the simulation under each HNP, following the same setting in (Yue et al., 2022). Specifically, instead of creating all agents at the same time, we initiate agents batch by batch from the boundaries so that they start with no collisions and walk into the scene. For 30-second simulations, we divide the time into $t = 0$ to 8, $t = 4$ to 12, and $t = 8$ to 16, where the density in the central area is the highest during $t=8$ to 16.

We report the average collision rates of three intervals in each simulation for every method in Fig. 5. Overall, BNSP-SFM and NSP-SFM outperform the baseline methods with lower collision rates across different agent numbers. To further understand it, we show detailed collision rates on

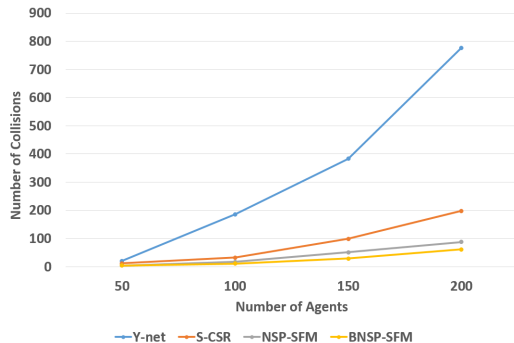


Fig. 7 The relationship between the number of collisions and the number of agents. Our BNSP-SFM outperforms other baseline methods in the number of collisions.

three intervals for all methods in Fig. 6 when HNP=200. Y-net performs poorly in all three time intervals. This indicates that, from the very beginning, collisions start to happen. Comparatively, S-CSR performs better, especially in the beginning when the agents start to walk into the scene. However, its collision rate spikes to 2% when the density becomes the highest. Comparatively, BNSP-SFM and NSP-SFM perform well in every time interval. Although their collision rates also increase, the highest is only 0.8% for NSP-SFM and 0.5% for BNSP-SFM. On average, Y-net, S-CSR, and NSP-SFM are 1400%, 300%, and 66.67% worse than BNSP-SFM.

Collision rate does not directly reflect the number of collisions. In safety-critical applications, every collision should count. Therefore, we also show the averaged number of collisions of three intervals in each simulation experiment in Fig. 7. All models have more collisions when the density becomes higher. However, our BNSP-SFM model maintains the lowest collision number across all simulation settings. The closest second is NSP-SFM. Moreover, BNSP-SFM also shows the lowest increase rate of collisions when the density increases. Overall, we demonstrate that BNSP-SFM and NSP-SFM possess the strongest generalization to high-density scenarios through collision rates and the number of collisions. The repulsive force in our explicit model plays a key role in collision avoidance.

4.4 Explainability of Prediction

Being able to explain behaviors is crucial in human trajectory forecasting (Helbing & Molnár, 1995;

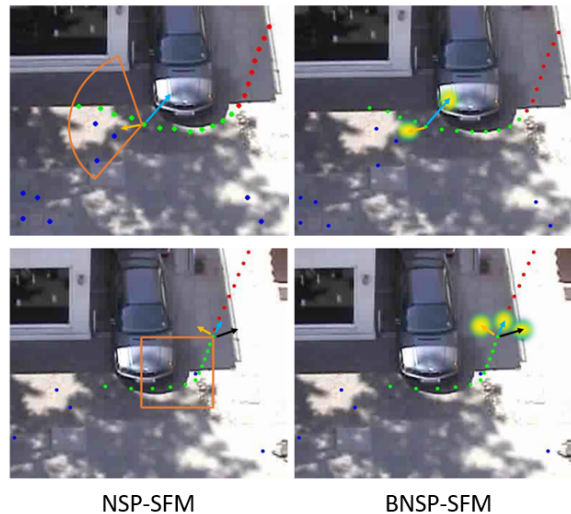


Fig. 8 Explainability of Behaviors. Red, blue, and green dots denote observations, neighbors, and predictions respectively. Main factors \mathcal{F}_{goal} , \mathcal{F}_{col} , and \mathcal{F}_{env} are shown as yellow, light blue, and black arrows for a pedestrian. The orange areas are two view fields in (Yue et al., 2022). The major difference between BNSP-SFM and NSP-SFM is the confidence in the factors shown as heatmaps.

Wang et al., 2016b). Our BNSP-SFM not only provides a plausible interpretation for pedestrian behaviors, but also gives the confidence of the interpretation. To this end, we analyze the three main factors \mathcal{F}_{goal} , \mathcal{F}_{col} , \mathcal{F}_{env} in the behavioral model, all of which are Gaussians. We demonstrate several explainability examples and compare this model with NPS-SFM (Yue et al., 2022).

In Fig. 8, we choose pedestrians with similar trajectories predicted by BNSP-SFM and NSP-SFM. In the top row, the pedestrian steers to avoid other pedestrians instead of going directly towards the goal. Both methods explain the steering by the influence of the goal attraction and the collision avoidance (yellow and blue arrows). However, BNSP-SFM also gives the confidence of the explanation, shown as heatmaps based on the learned means and variances of different factors. This not only gives the possible alternative explanations, but also shows how confident BNSP-SFM is regarding each explanation.

Fig. 8 Bottom shows a slightly more complex explanation where there is also environment repulsion (black arrow). The agent is attracted by his/her destination (yellow arrow) while he/she avoids collisions with other pedestrians (light blue

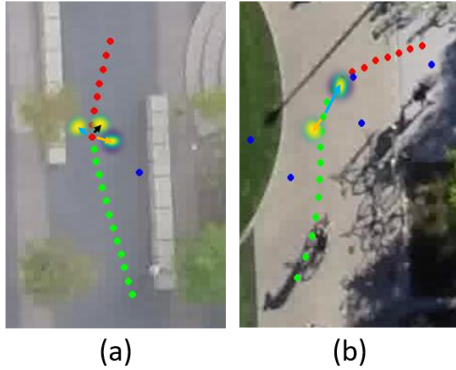


Fig. 9 Explainability of Behaviors. Red, blue, and green dots denote observations, neighbors, and predictions, respectively. Main factors \mathcal{F}_{goal} , \mathcal{F}_{col} , \mathcal{F}_{env} are shown as yellow, light blue, and black arrows for a pedestrian. The confidence in the factors is shown as heatmaps.

arrow) and is repelled by the obstacle car in the environment (black arrow). When there are multiple factors involved, the confidence maps associated with factors are more informative in terms of their relative confidence in our model. The environment repulsion arises when the person is very close to the car and avoiding the collision becomes a major concern. This is reflected by the environment repulsion having a more concentrated confidence map than the goal attraction and the collision avoidance. To be specific, the standard deviations for the factors \mathcal{F}_{goal} , \mathcal{F}_{col} , and \mathcal{F}_{env} here are [9.13, 11.40], [5.73, 8.14], [5.29, 2.02], respectively. Two standard deviations for each factor correspond to x-axis and y-axis. This means BNSP-SFM is more certain about the influence of the environment repulsion.

Overall, both NSP-SFM and BNSP-SFM give similar predicted trajectories with great prediction accuracy. Both methods can explain the same three factors. However, the means and the variances of the estimated distributions of social forces in BSNP-SFM provide more informative and explainable predictions.

We show more explainability examples of our BNSDE model in Fig. 9. The future trajectories (green dots) are predicted by using the standard sampling, where the \mathcal{F}_{goal} dominates among the three factors and has a more concentrated confidence map, shown in Fig. 9 (a). This is likely because there are not many imminent collisions for this person. With the more concentrated confidence map, BNSP-SFM is more certain about the

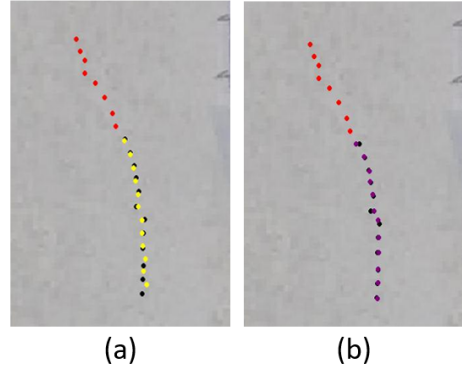


Fig. 10 Aleatoric and epistemic uncertainty. Red and black dots denote observations and the ground truth future trajectory. Yellow dots denote the prediction with only aleatoric uncertainty. Purple dots denote the prediction with aleatoric and epistemic uncertainty.

attraction of the destination, and the predicted future trajectory goes almost straight to the destination. In Fig. 9 (b), we ignore the influence of environment \mathcal{F}_{env} because it's too weak to be visualized here. \mathcal{F}_{col} dominates and has a more concentrated confidence map, meaning that our BNSP-SFM model is more certain about collision avoidance. This is because the neighbor in front of the person is walking at a high speed. The predicted future trajectory first avoids the neighbor then aims for the destination.

In human trajectory forecasting, to our best knowledge, few deep learning methods (Hossain et al., 2022; Kreiss, 2021; Yue et al., 2022) can provide explainability. In theory, we can also visualize black-box deep learning methods such as latent features or layer activations. However, it's difficult to determine how to visualize them to explain the behaviors. Among the explainable models, BNSP-SFM models the fine-grained structure of commonly observed uncertainty (He et al., 2020) and is therefore more explainable.

4.5 Epistemic Uncertainty

Fig. 10 shows how the BNSP-SFM model captures epistemic uncertainty as a residual of the predicted behavior with the aleatoric uncertainty. There are no neighbors or obstacles. The predicted trajectories in Fig. 10 (yellow and purple dots) are based on ultra-sampling. We capture only aleatoric uncertainty in Fig. 10 (a). We can see that the yellow dots are close to the ground truth (black dots), showing partial uncertainty has

Table 7 Results on partial training data of SDD based on ultra-sampling. XX/XX is ADE/FDE. All methods are trained using partial training data of SDD (from 25% to 100%) and are tested on the original testing data of SDD.

	S-CSR	NSP-SFM	BNSP-SFM (Ours)
Full SDD	2.77/3.45	1.78/3.44	1.52/1.37
50 % SDD	3.78/5.09	2.03/4.15	1.89/1.80
25 % SDD	4.60/6.44	2.10/4.32	2.01/2.00

been captured. BNSP-SFM exploits CVAE to capture the remaining epistemic uncertainty. Purple dots in Fig. 10 (b) denote the prediction with both the aleatoric and the epistemic uncertainty and almost overlap with the ground truth. This means that our model can capture the complete uncertainty well.

4.6 Data Efficiency

For human trajectory forecasting, it is expensive and time-consuming to collect clean data, which might involve manual labelling and checking. Therefore, data efficiency is crucial. We conduct experiments to test the data efficiency. We decrease the training data of SDD to 50% and 25%, then train BNSP-SFM, NSP-SFM, and S-CSR and test them on the original testing data of SDD. The results are shown in Tab. 7.

Both BNSP-SFM and NSP-SFM have higher data efficiency than S-CSR. Intuitively, this is sensible. When there is little data, black-box deep neural networks like S-CSR will be under-trained or overfitted. Having an explicit model in neural nets significantly reduces the required data size, which is known in differentiable physics models as explicit models can act as regularizers in learning (Gong et al., 2022). Both NSP-SFM and BNSP-SFM benefit from it.

Between NSP-SFM and BNSP-SFM, BNSP-SFM has less performance deterioration when the training data is reduced. This is because BNSP-SFM learns distributions of social forces, while NSP-SFM learns deterministic forces. Once the distributions are learned, it is still possible to sample good predictions, while NSP-SFM needs enough data to accurately learn the forces across space and time.



(a)

(b)

Fig. 11 Failure cases from the BNSP-SFM model. Red, green, and black dots denote the observations, predictions, and the ground truth future trajectories. (a) The goal prediction has high error leading to an overall low-quality prediction. (b) the pedestrian suddenly stopped resulting in zero velocity for a number of frames. Such behaviors are not captured very well as the goal attraction drags the pedestrian to move around the goal before it completely stop there.

4.7 Analysis of Failure Cases

Despite achieving the state-of-the-art performance in multiple applications, there are two sources of prediction error that BNSP-SFM can struggle to mitigate. Similar to deterministic SFM models, our model relies on the destination, which, if predicted wrong, can cause high overall prediction error, shown in Fig. 11 (a). This is decided by the overall explicit nature of BNSP-SFM, i.e. assuming the overall movement trend is largely decided by the force leading to the destination. A more fine-grained modeling of the destination could improve the results. Also, BNSP-SFM cannot predict well on highly nonlinear motions which is rare in the data employed. This is shown in Fig. 11 (b) where the pedestrian suddenly stopped, giving near-zero velocities in a number of frames. In this case, the goal attraction force can cause the agent to overshoot in reaching the goal. As a result, the agent moves around the goal for some time before being able to completely stop there. Such sudden stop behaviors also cause issues in simulators where some heuristics are needed to make the agent to stop as soon as they reach their goals. We do not employ similar heuristics as we mainly target prediction in this paper.

4.8 Ablation Study

To further understand the different components in our model, we conduct ablation experiments on SDD, shown in Tab. 8. We can see that our

Table 8 Ablation study on SDD. XX/XX is ADE/FDE.

\mathcal{F}_{att}	✓	✓	✓	✓
\mathcal{F}_{eva}	✗	✓	✓	✓
\mathcal{F}_{env}	✗	✓	✓	✓
Aleatoric	✗	✗	✓	✓
Epistemic	✗	✗	✗	✓
BNSP-SFM	6.52/10.57	6.46/10.49	2.32/2.66	1.52/1.37
NSP-SFM	6.57/10.68	6.52/10.61	n/a	1.78/3.44

model can obtain good results when only considering \mathcal{F}_{goal} because this is the goal attraction, which already determines the motion trend and governs the motion dynamics. \mathcal{F}_{col} and \mathcal{F}_{env} might not exist if there is no imminent collision with other pedestrians or the environment. However, we still obtain more accurate results by considering them.

Next, significant improvement is obtained by incorporating the aleatoric uncertainty. This demonstrates that our aleatoric model can capture the dynamics stochasticity well, meaning the aleatoric uncertainty is also a large source of prediction error. Note that the aleatoric uncertainty is modeled at the force level which further models the social interactions. Capturing such interaction uncertainty significantly improves the prediction.

Finally, we gain an even better result 1.52/1.37 by combining aleatoric and epistemic uncertainty. The total uncertainty is captured well by exploiting the excellent data-fitting capacity of deep learning. We can see that the performance improvement trend is similar for both BNSP-SFM and NSP-SFM in Tab. 8. This is because these two methods model the same three factors; the major difference is where the uncertainty is captured. To show the importance of fine-grained modeling of uncertainty, we compare BNSP-SFM with NSP-SFM. One noticeable result is that NSP-SFM also improves when uncertainty is captured, jumping from 6.52/10.61 to 1.78/3.44. However, such a gain is obtained by blindly fitting a neural network to capture the combined aleatoric and epistemic uncertainty. Consequently, not only is the uncertainty unexplainable, the overall performance is also slightly worse.

5 Discussion, Conclusion and Future Work

We have proposed a novel Bayesian neural stochastic differentiable equation model for

human trajectory forecasting. BNSP-SFM outperforms existing methods, achieving higher prediction accuracy, better generalizability, more explainability and higher data efficiency. One limitation is that our model does not explicitly consider high-level factors such as affective states in crowd dynamics, as studied in crowd research, which has found be to closely relevant to the motion randomness. In future, we will incorporate high-level factors, including the affective state, for better explainability. Moreover, we will explore our model in other areas such as autonomous vehicles and social robots.

6 Acknowledgment

This project has received funding from the European Union’s Horizon 2020 research and innovation programme under grant agreement No 899739 CrowdDNA.

Declarations

- Funding. This project has received funding from the European Union’s Horizon 2020 research and innovation programme under grant agreement No 899739 CrowdDNA.
- Conflict of interest/Competing interests (check journal-specific guidelines for which heading to use). Not applicable
- Ethics approval. Not applicable
- Consent to participate. Not applicable
- Consent for publication. All authors have given their consent for publication.
- Availability of data and materials. Data sharing not applicable to this article as no datasets were generated during the current study.
- Code availability. The code will be shared upon acceptance. Part of the code has been shared at <http://drhewang.com/pages/NSP.html>
- Authors’ contributions. Jiangbei Yue contributed in conceptualization, experiment design, conducting experiments and drafting the paper. Dinesh Manocha contributed in conceptualization and paper drafting. He Wang led the whole research project, including conceptualizing the research idea, supervision, drafting the paper, etc.

References

- Alahi, A., Goel, K., Ramanathan, V., Robicquet, A., Fei-Fei, L., Savarese, S. (2016). Social lstm: Human trajectory prediction in crowded spaces. *Proceedings of the IEEE conference on computer vision and pattern recognition* (pp. 961–971).
- Bartoli, F., Lisanti, G., Ballan, L., Del Bimbo, A. (2018). Context-aware trajectory prediction. *2018 24th international conference on pattern recognition (icpr)* (pp. 1941–1946).
- Bendali-Braham, M., Weber, J., Forestier, G., Idoumghar, L., Muller, P.-A. (2021). Recent trends in crowd analysis: A review. *Machine Learning with Applications*, 4, 100023.
- Bennewitz, M., Burgard, W., Thrun, S. (2002). Learning motion patterns of persons for mobile service robots. *Proceedings 2002 IEEE international conference on robotics and automation (cat. no. 02ch37292)* (Vol. 4, pp. 3601–3606).
- Blundell, C., Cornebise, J., Kavukcuoglu, K., Wierstra, D. (2015). Weight uncertainty in neural network. *International conference on machine learning* (pp. 1613–1622).
- Deo, N., & Trivedi, M.M. (2020). Trajectory forecasts in unknown environments conditioned on grid-based plans. *arXiv preprint arXiv:2001.00735*.
- Dietrich, F., Makeev, A., Kevrekidis, G., Evangelou, N., Bertalan, T., Reich, S., Kevrekidis, I.G. (2021). Learning effective stochastic differential equations from microscopic simulations: combining stochastic numerics and deep learning. *arXiv preprint arXiv:2106.09004*.
- Ferrer, G., & Sanfeliu, A. (2014). Behavior estimation for a complete framework for human motion prediction in crowded environments. *2014 IEEE international conference on robotics and automation (icra)* (pp. 5940–5945).
- Giuliari, F., Hasan, I., Cristani, M., Galasso, F. (2021). Transformer networks for trajectory forecasting. *2020 25th international conference on pattern recognition (icpr)* (pp. 10335–10342).
- Gong, D., Zhu, Z., Andrew, B., Wang, H. (2022). Fine-grained differentiable physics: a yarn-level model for fabrics. *International conference on learning representations*.
- Goodfellow, I., Pouget-Abadie, J., Mirza, M., Xu, B., Warde-Farley, D., Ozair, S., ... Bengio, Y. (2020). Generative adversarial networks. *Communications of the ACM*, 63(11), 139–144.
- Gupta, A., Johnson, J., Fei-Fei, L., Savarese, S., Alahi, A. (2018). Social gan: Socially acceptable trajectories with generative adversarial networks. *Proceedings of the IEEE conference on computer vision and pattern recognition* (pp. 2255–2264).
- He, F., Xia, Y., Zhao, X., Wang, H. (2020). Informative scene decomposition for crowd analysis, comparison and simulation guidance. *ACM Transaction on Graphics (TOG)*, 4(39).
- Helbing, D., & Molnár, P. (1995). Social force model for pedestrian dynamics. *Phys. Rev. E*, 51, 4282–4286.
- Hochreiter, S., & Schmidhuber, J. (1997). Long short-term memory. *Neural computation*, 9(8), 1735–1780.
- Hossain, S., Johora, F.T., Müller, J.P., Hartmann, S., Reinhardt, A. (2022). SFMGNet: A Physics-based Neural Network To Predict Pedestrian Trajectories. *Proceedings of the AAAI spring symposium on machine learning and knowledge engineering for hybrid intelligence (aaai-make)* (pp. 1–16).

Retrieved from <https://proceedings.aaai-make.info/AAAI-MAKE-PROCEEDINGS-2022/paper14.pdf>

- Huang, X., McGill, S.G., Williams, B.C., Fletcher, L., Rosman, G. (2019). Uncertainty-aware driver trajectory prediction at urban intersections. *2019 international conference on robotics and automation (icra)* (pp. 9718–9724).
- Ivanovic, B., & Pavone, M. (2019). The trajectron: Probabilistic multi-agent trajectory modeling with dynamic spatiotemporal graphs. *Proceedings of the IEEE/CVF International Conference on Computer Vision* (pp. 2375–2384).
- Jospin, L.V., Laga, H., Boussaid, F., Buntine, W., Bennamoun, M. (2022). Hands-on bayesian neural networks—a tutorial for deep learning users. *IEEE Computational Intelligence Magazine*, 17(2), 29–48.
- Karniadakis, G.E., Kevrekidis, I.G., Lu, L., Perdikaris, P., Wang, S., Yang, L. (2021). Physics-informed machine learning. *Nature Reviews Physics*, 3(6), 422–440.
- Kim, S., Guy, S.J., Liu, W., Lau, R.W., Lin, M.C., Manocha, D. (2013). Predicting pedestrian trajectories using velocity-space reasoning. *Algorithmic foundations of robotics x* (pp. 609–623). Springer.
- Kingma, D.P., Welling, M., et al. (2019). An introduction to variational autoencoders. *Foundations and Trends® in Machine Learning*, 12(4), 307–392.
- Kosaraju, V., Sadeghian, A., Martín-Martín, R., Reid, I., Rezatofghi, H., Savarese, S. (2019). Social-bigat: Multimodal trajectory forecasting using bicycle-gan and graph attention networks. *Advances in Neural Information Processing Systems*, 32.
- Kreiss, S. (2021). Deep social force. *arXiv preprint arXiv:2109.12081*.
- Lerner, A., Chrysanthou, Y., Lischinski, D. (2007). Crowds by example. *Computer graphics forum* (Vol. 26, pp. 655–664).
- Li, X., Wong, T.-K.L., Chen, R.T., Duvenaud, D. (2020). Scalable gradients for stochastic differential equations. *International conference on artificial intelligence and statistics* (pp. 3870–3882).
- Liang, J., Jiang, L., Hauptmann, A. (2020). Simgaug: Learning robust representations from 3d simulation for pedestrian trajectory prediction in unseen cameras. *arXiv preprint arXiv:2004.02022*, 2.
- Liang, J., Jiang, L., Niebles, J.C., Hauptmann, A.G., Fei-Fei, L. (2019). Peeking into the future: Predicting future person activities and locations in videos. *Proceedings of the IEEE/CVF Conference on Computer Vision and Pattern Recognition* (pp. 5725–5734).
- Luo, L., Zhou, S., Cai, W., Low, M.Y.H., Tian, F., Wang, Y., . . . Chen, D. (2008). Agent-based human behavior modeling for crowd simulation. *Computer Animation and Virtual Worlds*, 19(3-4), 271–281.
- Mangalam, K., An, Y., Girase, H., Malik, J. (2021). From goals, waypoints & paths to long term human trajectory forecasting. *Proceedings of the IEEE/CVF International Conference on Computer Vision* (pp. 15233–15242).
- Mangalam, K., Girase, H., Agarwal, S., Lee, K.-H., Adeli, E., Malik, J., Gaidon, A. (2020). It is not the journey but the destination: Endpoint conditioned trajectory prediction. *European conference on computer vision* (pp. 759–776).

- Mohamed, A., Qian, K., Elhoseiny, M., Claudel, C. (2020). Social-stgcn: A social spatio-temporal graph convolutional neural network for human trajectory prediction. *Proceedings of the IEEE/CVF conference on computer vision and pattern recognition* (pp. 14424–14432).
- Narang, S., Best, A., Curtis, S., Manocha, D. (2015). Generating pedestrian trajectories consistent with the fundamental diagram based on physiological and psychological factors. *PLoS one*, 10(4), e0117856.
- Opper, M. (2019). Variational inference for stochastic differential equations. *Annalen der Physik*, 531(3), 1800233.
- Pellegrini, S., Ess, A., Gool, L.V. (2010). Improving data association by joint modeling of pedestrian trajectories and groupings. *European conference on computer vision* (pp. 452–465).
- Robicquet, A., Sadeghian, A., Alahi, A., Savarese, S. (2016). Learning social etiquette: Human trajectory understanding in crowded scenes. *European conference on computer vision* (pp. 549–565).
- Sadeghian, A., Kosaraju, V., Sadeghian, A., Hirose, N., Rezaatofghi, H., Savarese, S. (2019). Sophie: An attentive gan for predicting paths compliant to social and physical constraints. *Proceedings of the IEEE/CVF conference on computer vision and pattern recognition* (pp. 1349–1358).
- Schneider, N., & Gavrilu, D.M. (2013). Pedestrian path prediction with recursive bayesian filters: A comparative study. *german conference on pattern recognition* (pp. 174–183).
- Shen, S., Yang, Y., Shao, T., Wang, H., Jiang, C., Lan, L., Zhou, K. (2021, jul). High-order differentiable autoencoder for nonlinear model reduction. *ACM Trans. Graph.*, 40(4).
- Shi, L., Wang, L., Long, C., Zhou, S., Zhou, M., Niu, Z., Hua, G. (2021). Sgc: Sparse graph convolution network for pedestrian trajectory prediction. *Proceedings of the IEEE/CVF conference on computer vision and pattern recognition* (pp. 8994–9003).
- Thrun, S., Burgard, W., Fox, D. (2005). *Probabilistic robotics (intelligent robotics and autonomous agents series), ser. intelligent robotics and autonomous agents*. The MIT Press.
- Tzen, B., & Raginsky, M. (2019). Neural stochastic differential equations: Deep latent gaussian models in the diffusion limit. *arXiv preprint arXiv:1905.09883*.
- Vemula, A., Mueller, K., Oh, J. (2018). Social attention: Modeling attention in human crowds. *2018 IEEE international conference on robotics and automation (ICRA)* (pp. 4601–4607).
- Wang, H., Ondřej, J., O’Sullivan, C. (2016a). Path patterns: Analyzing and comparing real and simulated crowds. *Acm siggraph symposium on interactive 3d graphics and games 2016* (pp. 49–57).
- Wang, H., Ondřej, J., O’Sullivan, C. (2016b). Trending paths: A new semantic-level metric for comparing simulated and real crowd data. *IEEE Transactions on Visualization and Computer Graphics*, PP(99), 1-1.
- Wang, H., & O’Sullivan, C. (2016). Globally continuous and non-markovian crowd activity analysis from videos. *European conference on computer vision* (pp. 527–544).
- Wong, C., Xia, B., Hong, Z., Peng, Q., Yuan, W., Cao, Q., ... You, X. (2022). View vertically: A hierarchical network for trajectory prediction via fourier spectrums. *European conference on computer vision* (pp. 682–700).
- Xu, P., Hayet, J.-B., Karamouzas, I. (2022). Socialvae: Human trajectory prediction

using timewise latents. *arXiv preprint arXiv:2203.08207*.

- Yan, X., Kakadiaris, I.A., Shah, S.K. (2014). Modeling local behavior for predicting social interactions towards human tracking. *Pattern Recognition*, 47(4), 1626–1641.
- Yu, C., Ma, X., Ren, J., Zhao, H., Yi, S. (2020). Spatio-temporal graph transformer networks for pedestrian trajectory prediction. *European conference on computer vision* (pp. 507–523).
- Yue, J., Manocha, D., Wang, H. (2022). Human trajectory prediction via neural social physics. *Proceedings of the european conference on computer vision (eccv)*.
- Zhang, P., Ouyang, W., Zhang, P., Xue, J., Zheng, N. (2019). Sr-lstm: State refinement for lstm towards pedestrian trajectory prediction. *Proceedings of the ieee/cvf conference on computer vision and pattern recognition* (pp. 12085–12094).
- Zhang, Z., Jimack, P.K., Wang, H. (2021, July). MeshingNet3D: Efficient generation of adapted tetrahedral meshes for computational mechanics. *Advances in Engineering Software*, 157-158.
- Zhang, Z., Wang, Y., Jimack, P.K., Wang, H. (2020). Meshingnet: A new mesh generation method based on deep learning. *Computational science – iccs 2020* (pp. 186–198). Cham: Springer International Publishing.
- Zhou, H., Ren, D., Yang, X., Fan, M., Huang, H. (2021). Sliding sequential cvae with time variant socially-aware rethinking for trajectory prediction. *arXiv preprint arXiv:2110.15016*.